

Electrochemical-thermal modeling and experimental validation of commercial graphite/LiFePO₄ pouch lithium-ion batteries

Mehrdad Mastali^{a,*}, Evan Foreman^b, Ali Modjtahedi^b, Ehsan Samadani^a, Amir Amirfazli^b, Siamak Farhad^b, Roydon A. Fraser^a, Michael Fowler^c

^a Mechanical and Mechatronic Engineering Department, University of Waterloo, 200 University Ave. West, Waterloo, ON, N2L 3G1, Canada

^b Mechanical Engineering Department, University of Akron, Akron, OH 44325, United States

^c Chemical Engineering Department, University of Waterloo, 200 University Avenue West, Waterloo, ON, N2L 3G1, Canada

ARTICLE INFO

Keywords:

Graphite/LiFePO₄ lithium-ion battery
Large-sized commercial pouch battery
Coupled electrochemical-thermal model
Experimental validation
Temperature distribution
Tab heating effect

ABSTRACT

Large-sized lithium-ion battery (LIB) mathematical models are critical in design of cells, packs, and their associated thermal management systems. A high-fidelity fully coupled electrochemical-thermal model for a commercial 20 Ah LIB is developed to simulate the distribution of electrochemical and thermal variables three-dimensionally (3D) through 48 electrode layers in the pouch cell. As a new feature, the details of heat generation and voltage drop due to the tab, current collectors, and associated contact resistances are included in the developed model. A series of galvanostatic charge/discharge tests at operating rates ranging from 1C (20 A) to 5C (100 A) and at room temperature is conducted on the pouch cell and the output voltage and temperature distribution are recorded. The developed model voltage and temperature distribution predictions are successfully compared against the experimental data, demonstrating the accuracy of the model. As a key finding in this work, it is found that self-heating is the main contributor for electrochemical performance improvement in large-sized LIBs over small cells. This is due to the improved kinetic and transport properties of LIB electrodes at elevated temperatures. It is also demonstrated that the temperature variation between the surface and center layers of a pouch cell is not significant at a maximum difference of about 1.7 °C for charge/discharge rates up to 5C (100 A). As a result of this finding, it is suggested that a single temperature measurement close to the tabs at the battery surface would be sufficient for thermal management development and control purposes.

1. Introduction

Due to their high specific energy and power density, large-sized lithium-ion batteries (LIBs) have gained a lot of interest as an energy storage solution for electrified vehicles and smart electrical grid applications. However, using these LIBs brings about new challenges such as thermal management since the operating temperature of the LIBs significantly affect their performance, durability, and safety [1,2]. It has been shown that elevated temperatures accelerate the LIBs capacity fade during storage and under cycling conditions [3]. In addition, lack of a proper thermal management would result in thermal runaway in some extreme conditions, such as harsh charging/discharging cycles [4], and also internal short circuit [5]. As a result, a rugged thermal management is vital in order to prevent high temperatures and overheating during the LIB operation, especially in case of large-sized batteries.

There are two main approaches in thermal management of LIBs:

decreasing the heat generation inside the battery, and improving the heat dissipation from the battery. In the first approach, the electrochemical performance of the cell is improved by reducing the internal resistance of the battery. Different methods such as altering the thickness of the electrodes [6], changing the active material particle size [7], and modifying the negative [8] and positive [9] electrodes have been incorporated so far. In the latter approach, the heat transfer from the battery to the environment is optimized in order to reduce the maximum temperature of the battery and make the temperature distribution more uniform. To this end, four types of thermal management systems based on air cooling [10], liquid cooling [11], heat pipe cooling [12], and phase-change-material cooling [13] have been developed. To accelerate the design process of battery cells and packs as well as thermal management systems, however, developing high-fidelity models to predict the electrochemical-thermal behavior of LIBs would be necessary. These models provide a framework to study the effect of each parameter on the battery thermal and electrochemical behavior

* Corresponding author.

E-mail address: mmastali@uwaterloo.ca (M. Mastali).

with no need to run costly and time-consuming experimental tests or prototyping. In addition, using such models, valuable information about LIB internal phenomena, which is not easily accessible through experiments, would become available.

Different mathematical models, including equivalent circuit models (ECMs) [14,15] and physics-based one-dimensional (1D) models [16], have been developed for LIB simulations. However, the non-uniformities observed in the distribution of large-sized LIB electrochemical and thermal variables are not captured in these simple models [17]. As an alternative approach, researchers combine ECMs with the three-dimensional (3D) charge conservation and heat diffusion equations yielding a 3D model of batteries [18]. This 3D model, however, has limited applicability due to the incorporated ECM shortcomings. In another work, Kwon et al. [19] develop a 3D model to study the current and voltage distributions in a lithium-polymer battery. In their model, the electrochemical equations are not included and instead, the internal resistance of the battery layers is identified from experimental data as a function of depth of discharge (DOD). Kim et al. [20] add a thermal sub-model to the Kwon's model in order to determine the surface temperature distribution of an LIB. However, in their model, the electrochemical and thermal sub-models are not fully coupled and the temperature distribution does not affect the electrochemical variables. In an attempt to couple the electrochemical and thermal models, Bandhauer et al. [21] use a series of fitted functions to the experimental data instead of an electrochemical model. Although this modeling approach is suitable for studying different thermal management strategies, it remains limited for the same reasons ECMs are limited, for example, lack of predictive ability. Therefore, a variety of models have been developed utilizing a physics-based electrochemical model instead of ECMs or fitting approaches. Most of these models assume uniform kinetics all over the electrodes and incorporate a single physics-based 1D model throughout the electrodes [22–24]. As a result, the distributions of electrochemical variables in the LIB are neglected while current and voltage variations are solved three-dimensionally. To overcome this drawback, few researchers utilize physics-based 1D models as a source term in the charge conservation and heat diffusion equations [25–29]. However, there is no comprehensive validation of their model against experimental data. Also, the layered geometry of the LIB is not resolved in their computational domain. These shortcomings will lead to a poor model fidelity and inaccurate fitting parameters. To address the aforementioned issues, in this paper a coupled electrochemical-thermal model for a commercial 20 Ah 48-layer pouch cell is developed and validated against experimental data. This high-fidelity model offers several advantages to the existing models, as it incorporates all the electrochemical-geometrical details of the cell and accounts for the heat generation in the tabs and other battery contact resistances.

2. Experimental

A LIB pouch cell [30], is used to verify model results. As shown in Fig. 1-a, the cell is held in the upright position by a two-clamp stand. Seven Omega HFS-4 thin-film heat flux sensors with built-in Type-K thermocouples (TC_1 to TC_7) are used to collect temperature data from the cell surface. Temperatures are measured on only one side of the pouch cell given its symmetric construction as described in Section 3. Also, two additional individual Type-K TCs are attached to the pouch cell terminals. The exact location of the thermocouples is given in Fig. 1-b.

Temperature versus time measurements from the nine pairs of TC wires are obtained using a National Instruments DAQ 9171 and National Instruments LabVIEW software [31]. A BioLogic Science Instruments BCS-815 battery cycler with a CC8 8-channel current collector [32] is used to apply the required current to the cell. Using BT-Lab software developed by BioLogic Science [33], a charge/discharge profile was created according to the following standard procedure: (i) first, charge the pouch cell at the desired constant C-rate (current), until

the voltage reaches the higher cut-off voltage of 3.7 V, (ii) then, continue to charge the pouch cell at a constant voltage of 3.7 V until the current drops below 200 mA, (iii) put the pouch cell at open circuit rest condition for 8 h, (iv) discharge the pouch cell at the desired constant C-rate (current), until the voltage reaches the lower cut-off voltage of 2.4 V, (v) continue to discharge the pouch cell at a constant voltage of 2.4 V until the current drops below 200 mA, and (vi) lastly, put the pouch cell at open circuit rest condition for 8 h. These 6 steps are repeated using C-rates (currents) of 1C (20 A), 2C (40 A), 3C (60 A), and 5C (100 A). Given the unknown state of the pouch cell before the 1C (20 A) discharge, an initial charge and discharge following the above procedure is first done for C/2 (10 A).

3. Model development

As illustrated in Fig. 2, the studied pouch cell includes a number of individual battery cells connected in parallel inside the casing. Each cell contains a negative electrode, a separator, and a positive electrode, surrounded on either side by the current collectors. In the pouch cell studied in this paper, the negative and positive electrodes active materials are made from graphite and $LiFePO_4$, respectively. Copper is used as the negative current collector and aluminum as the positive current collector. This pouch cell includes 48 individual cells resulting in a 20 Ah nominal capacity. In order to decrease the material demand and reduce the electrical losses, current collectors are covered by electrode materials on both sides. Therefore, the number of aluminum current collectors for 48 cells is 24, while there are 25 copper current collectors since copper collectors are on each end of the stack like that shown in Fig. 2 for a 6-cell stack. All the layers are then enclosed in a separator sheet, and a casing covers all the electrode and current collecting materials.

The method used here is similar to that used in an earlier work by the authors [34]. The method used to describe the 3D current distribution in a single cell is expanded in this work to multiple layers within the same pouch. The current flowing to the pouch cell is first divided between all 48 cells connected in parallel within the pouch and then enters the current collectors using tabs. The current entering the collectors distributes inside the current collector plate and then crosses active materials as explained in Ref. [34]. Due to the much higher electrical conductivity of metallic collectors compared to the active material layers, and also due to the thinness of active material layers, it is assumed that the current flow in the active material layers is effectively 1D, i.e., perpendicular to the current collector plate. However, it should be noted that in spite of the comparatively low electrical resistance of metallic collectors, the conductor resistance cannot be ignored since it is the source of the 3D distribution of the current crossing the active material layers. Fig. 3 displays the explained current distribution in the current collector and between the layers during discharge. As seen, current from the current collector goes into the active material layers on either side of the collector.

3.1. Electrochemical model

As explained in the previous section, current flows perpendicularly between the negative and positive current collector sheets. Therefore, a 1D electrochemical model is sufficient to relate the local current density and voltage variation across the battery active material layers. Generally, the pseudo two-dimensional (P2D) model proposed by Newman et al. [35] is utilized as the 1D electrochemical model. However, since most of the computational effort in pouch cell simulation stems from the 1D models [34], simplifying this model is very crucial in this work. In this paper, the simple homogenous pseudo two-dimensional (HP2D) model previously developed by Mastali et al. [34] is utilized. This model is the same as the P2D model but with the additional assumption of homogenous electrochemical reaction across the electrodes. It is shown that this model can decrease the solution time by

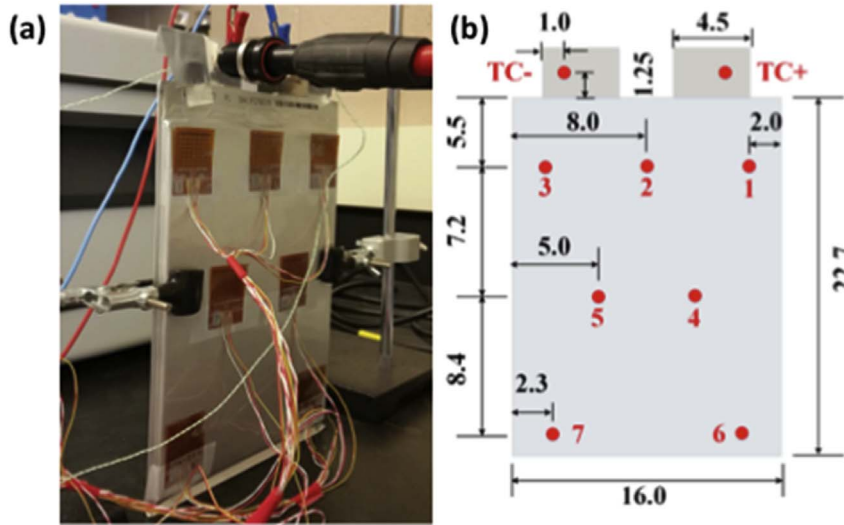


Fig. 1. (a) Pouch cell held in upright position with thermocouples attached. (b) Locations of thermocouples on the pouch cell, TC locations denoted by red '●' (all dimensions are in cm). TC₊ and TC₋ are located on the negative and positive cell terminals, respectively. (For interpretation of the references to colour in this figure legend, the reader is referred to the Web version of this article.)

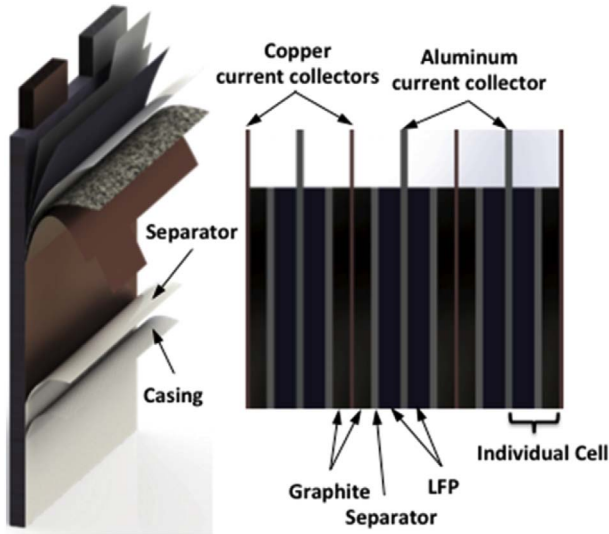


Fig. 2. Structure of the multi-cell LIB pouch cell.

one order of magnitude, with a maximum deviation of only 1.5%, compared to the P2D model [34]. Since the studied pouch cell in this paper contains graphite as the negative and LiFePO₄ as the positive

electrodes, the phase change process in the active materials is captured using a variable solid-state diffusivity (VSSD) model [36]. This paper is not aimed at developing 1D models; thus, model details are not discussed here and can be found in Ref. [36]. The governing equations, and corresponding boundary and initial conditions, are summarized in Table 1. It should be mentioned that the particle-level equations are separately applied to both negative and positive electrodes. Variable definitions are given in the nomenclature and Ref. [36]. The input to the 1D model is the local normal current density, j_n , and the output is the voltage variation across the active material layers, $\nabla\phi_{lay}$, calculated from Equation (1):

$$\nabla\phi_{lay} = \phi_s|_{x=L} - \phi_s|_{x=0} - R_c j_n \quad (1)$$

where L is the cell thickness of active material layers (separator plus the electrodes).

3.2. Electrical model

To calculate the current and voltage distributions in the pouch cell, the model presented in Ref. [34], which is applicable to only one individual cell or layer within a pouch, is expanded here. For more explanation regarding the resistor network analogy used to model the electrical behavior of one individual cell, the reader is advised to refer to Section 3 of [34]. To expand the one cell electrical model to multi-layer pouch cell electrical model, the current flow from both sides of the

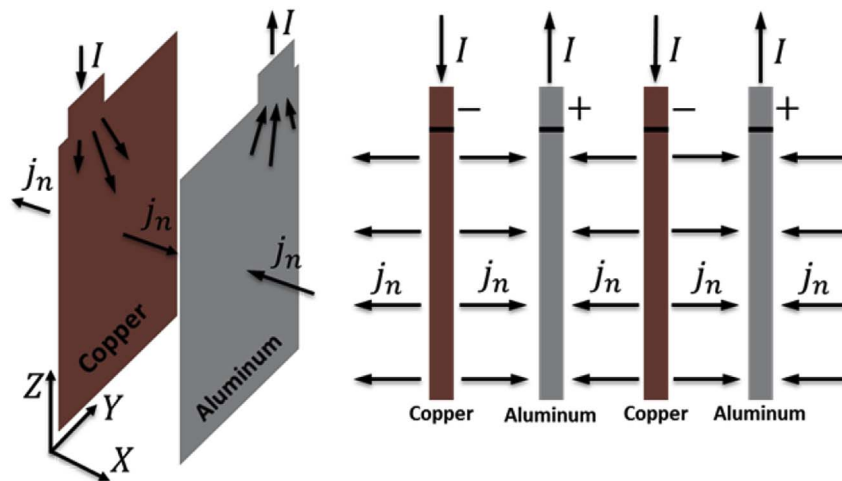


Fig. 3. Current and current density distribution in the LIB electrodes during the discharge.

Table 1

The governing equations and corresponding boundary conditions of the homogenous pseudo-two-dimensional (HP2D) model.

Particle-level governing equations	
Anode/Cathode active materials	Boundary and initial conditions
$\frac{\partial c_{s,k}}{\partial t} = \frac{1}{r_k^2} \frac{\partial}{\partial r_k} \left(r_k^2 \alpha_k \frac{\partial c_{s,k}}{\partial r_k} \right) \alpha_k = -\frac{F}{RT} y_k (1 - y_k) \frac{\partial U_k}{\partial y_k}, y_k = c_{s,k}/c_s^{max}$ $i_{n,k} = 2i_k^0 \left[\exp\left(\frac{(1-\beta)F}{RT} \eta_k\right) - \exp\left(\frac{-\beta F}{RT} \eta_k\right) \right] j_n = L_i \sum a_k i_{n,k} \eta_k = \phi_s - \phi_e - U_k, a_k = 3\varepsilon_k/R_{p,k} i_k^0 = Fk^0 c_e^{1-\beta} c_s^{max} (1 - y_k)^{1-\beta} y_k^\beta$	$\left. \frac{\partial c_{s,k}}{\partial r_k} \right _{r_k=0} = 0 \alpha_k \frac{\partial c_{s,k}}{\partial r_k} \bigg _{r_k=R_{p,k}} = \frac{i_{n,k}}{F} c_{s,k} _{t=0} = c_{s,k}^0$
Electrode-level governing equations	
Battery layers	Boundary and initial conditions
$\nabla \cdot (\sigma_i^{eff} \nabla \phi_s) = H_i, i = a, s, c \sigma_i^{eff} = \sigma_i (1 - \varepsilon_i)^\gamma$ $\nabla \cdot (-\kappa_i^{eff} \nabla \phi_e) + \nabla \cdot (\kappa_{D,i}^{eff} \nabla \ln c_e) = H_i, i = a, s, c \kappa_i^{eff} = \kappa_i \varepsilon_i^\gamma, \kappa_{D,i}^{eff} = \frac{2RT\kappa_i^{eff}}{F} (1 - t_+^0) \left(1 + \frac{d \ln f_{\pm}}{d \ln c_e} \right) H_a = \frac{j_n}{L_a}, H_s = 0, H_c = -\frac{j_n}{L_c}$ $\frac{\partial (q_{ce})}{\partial t} = \nabla \cdot (D_{e,i}^{eff} \nabla c_e) + \frac{1-t_+^0}{F} H_i, i = a, s, c D_{e,i}^{eff} = D_e \varepsilon_i^\gamma$	$\sigma_a^{eff} \nabla \phi_s _{x=L_a} = \sigma_c^{eff} \nabla \phi_s _{x=L_a+L_s} = 0$ $\sigma_c^{eff} \nabla \phi_s _{x=L} = j_n \phi_s _{x=0} = 0$ $\kappa_a^{eff} \nabla \phi_e _{x=0} = \kappa_c^{eff} \nabla \phi_e _{x=L} = 0$ <p>continuity at $x = L_a$ and $x = L_a + L_s$</p> $D_{e,a}^{eff} \nabla c_e _{x=0} = D_{e,c}^{eff} \nabla c_e _{x=L} = 0$ <p>continuity at $x = L_a$ and $x = L_a + L_s c_e _{t=0} = c_e^0$</p>

current collectors has to be taken into the account, except for the two copper collectors at each end of the LIB pouch cell. The charge conservation equation that applies to each current collector is thus arranged as follows, with the two copper collectors on the ending layers of the pouch cell having one of the right hand side terms set to zero:

$$\sigma_i \frac{\partial^2 \Phi_i}{\partial Y^2} + \sigma_i \frac{\partial^2 \Phi_i}{\partial Z^2} = \frac{j_{n,i-1}}{L_i} + \frac{j_{n,i+1}}{L_i} \quad (2)$$

where i shows the i^{th} current collector, Y and Z are coordinate systems as shown in Fig. 3, $j_{n,i-1}$ is the normal outward current density flowing between the i^{th} and $(i-1)^{th}$ current collectors, $j_{n,i+1}$ is the normal outward current density flowing between the i^{th} and $(i+1)^{th}$ current collectors, and L_i is the thickness of the current collectors.

The material and geometrical properties of the current collectors are known. The normal current densities are then replaced by the following linear relation:

$$j_n = a \nabla \phi_{lay} + b \quad (3)$$

where a and b are time and space varying linear relation coefficients, and $\nabla \phi_{lay}$ is the voltage gradient between the corresponding nodes on the positive and negative current collectors calculated using Equation (1). In order to calculate the value of these coefficients, two points are required for the current density and voltage gradient pair. To this end, the first point uses the calculated normal current density at the last time step and the second point uses a value close to the normal current density at the last time step. Given these current densities, the corresponding voltage gradients are then calculated using the 1D electrochemical models presented in Table 1 and Equation (1). In contrast to the approach used in Refs. [37,38] that ignores the voltage gradient along the current collectors, the coupling utilized here between the current and voltage distributions leads to the simultaneous calculation of these two variables at each time step.

The boundary conditions for Equation (2) are the zero reference voltage for all negative current collector tabs, and an equal but time varying electrical voltage for all positive tabs. It is also assumed that the current, I_i , at the top surface area of a positive current collector tab is evenly distributed spatially [34], but the current is allowed to be different for each tab. The total current through all positive current collector tabs sums to the total applied pouch cell current, I_{app} , as follows:

$$I_1 + I_2 + \dots + I_{23} + I_{24} = I_{app} \quad (4)$$

A zero-flux condition is considered for the remaining current

collector boundaries.

Applying the above boundary conditions, as well as Equation (3), the charge conservation equation (Equation (2)) can be solved for the voltage distribution in the pouch cell. Equation (3) is then used to calculate the normal current density distribution. By knowing the current density distribution, new values for the 1D model variables (electrochemical variables) can be determined. This process is repeated for the next time step to update the voltage distribution, normal current density distribution, and electrochemical variables until the lower cut-off voltage of the pouch cell (2.4 V) during the discharge or higher cut-off voltage (3.7 V) during the charge is reached.

3.3. Thermal model

3.3.1. Energy balance

The energy balance for the pouch cell is given by the heat diffusion equation:

$$\rho C_p \frac{\partial T}{\partial t} = \frac{\partial}{\partial X} \left(k_x \frac{\partial T}{\partial X} \right) + \frac{\partial}{\partial Y} \left(k_y \frac{\partial T}{\partial Y} \right) + \frac{\partial}{\partial Z} \left(k_z \frac{\partial T}{\partial Z} \right) + \dot{q}_{gen} \quad (5)$$

Equation (5) is separately applied to the active material layers, current collectors, and outside layer (the separator and casing) of the pouch cell. Note that the active material layers are treated as a single layer whose local temperature gradient normal to the current collector plates is negligible given the thinness of these layers and relatively high thermal conductivity of the contained materials [39].

The thermal model considers both convective and radiative heat transfers to the surrounding. These heat transfers are treated as the boundary conditions for Equation (5) and are expressed as follows:

$$\dot{q}_{conv} = h(T_{surf} - T_{amb}), \quad (6)$$

$$\dot{q}_{rad} = \sigma E(T_{surf}^4 - T_{amb}^4), \quad (7)$$

where σ is the Stefan-Boltzmann constant.

3.3.2. Heat generation

Heat generation in pouch cells originates from two different sources: heat generation in active material layers, and heat generation in the current collectors. The local heat generation rate in the active material layers, $\dot{q}_{gen,lay}$, is revised from Ref. [40] for HP2D model to reflect the homogeneity of the electrochemical reaction rate across the electrodes and is expressed as follows:

$$\begin{aligned} \dot{q}_{gen, lay} = & \sum_{l=n,p} \sum_k a_{k,l} i_{n,k,l} T \frac{\partial U_{k,l}}{\partial T} + \sum_{l=n,p} \sum_k a_{k,l} i_{n,k,l} (\phi_s - \phi_e - U_{k,l}) \\ & + \frac{1}{L} \int \left(\sigma^{eff} \left(\frac{\partial \phi_s}{\partial x} \right)^2 + \kappa^{eff} \left(\frac{\partial \phi_e}{\partial x} \right)^2 + \kappa_D^{eff} \left(\frac{\partial \ln c_e}{\partial x} \right) \left(\frac{\partial \phi_e}{\partial x} \right) \right) dx \\ & + \frac{R_c}{L} j_n^2 \end{aligned} \quad (8)$$

where L is the thickness of the active material layers (separator plus the electrodes).

In Equation (8), the first term on the right-hand-side is reversible entropic heat generation while the remaining terms are irreversible heat generation terms. Specifically, the second term represents the reaction heat generated on the surface of the negative and positive electrode particles, while the third term represents Joule heating due to movement of electrons and ions in the electrodes and electrolyte, respectively. Finally, the last term represents heat generated from contact resistance between the electrodes and current collectors. In contrast, the heat generated in the current collectors, $\dot{q}_{gen, cc,i}$, is only due to ohmic resistance in the current collectors and is formulated as follows [41]:

$$\dot{q}_{gen, cc,i} = \sigma_{cc,i} \left[\left(\frac{\partial \Phi_i}{\partial Y} \right)^2 + \left(\frac{\partial \Phi_i}{\partial Z} \right)^2 \right] \quad (9)$$

where i stands for negative or positive current collector.

3.3.3. Thermal properties

Given the layered nature of the active materials and outer layer, two different effective conductivities are used: k_{ser} , in the direction perpendicular to the layers, and k_{par} , parallel to the layers. Fig. 4 shows, for two active material layers, the series and parallel thermal circuits used for calculating effective conductivities based on thermal resistances.

Since the electrolyte fills the pores and gaps between the material particles and its thermal conductivity is comparable to that of particles, it is assumed that the contact resistances are negligible. Therefore, whenever two layers are connected in a series configuration (Fig. 4-a), the thermal conductivity, k_{ser} , is determined by:

$$k_{ser} = \frac{L_1 + L_2}{\left(\frac{L_1}{k_1} \right) + \left(\frac{L_2}{k_2} \right)}, \quad (10)$$

Also, whenever two layers are parallel (Fig. 4-b), the following equation provides the effective thermal conductivity, k_{par} :

$$k_{par} = \frac{A_1}{A_1 + A_2} k_1 + \frac{A_2}{A_1 + A_2} k_2 \quad (11)$$

In addition, since each layer is composed of different materials, such as conductive filler, polymer, and active material, the thermal conductivity of each layer, k_{layer} , is calculated based on the volume averaging as follows:

$$k_{layer} = \frac{\sum_i k_i V_i}{\sum_i V_i}, \quad (12)$$

The same volume weighted average method is used to calculate the

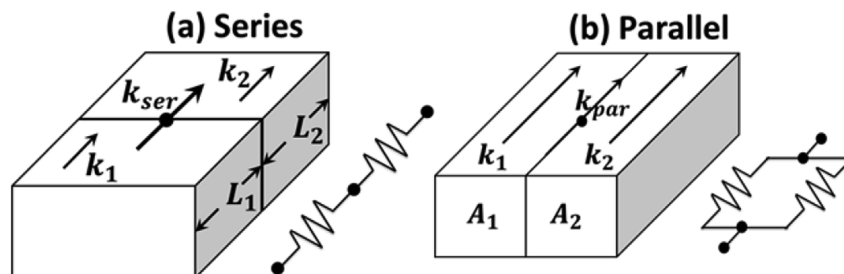


Fig. 4. Schematic representation of the effective thermal conductivity estimation when the layers are connected in (a) series or (b) parallel (based on [42]).

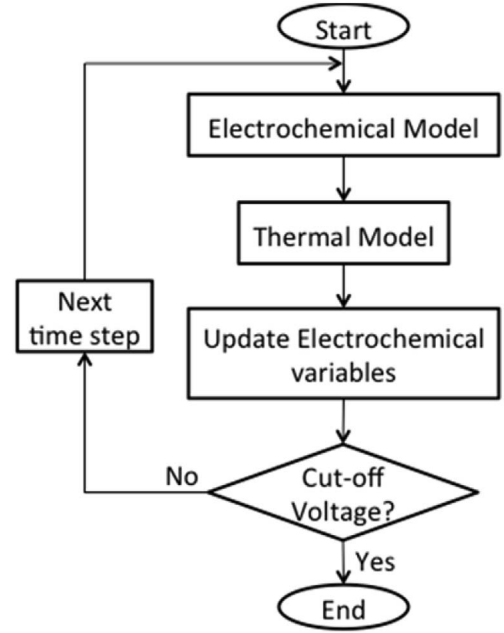


Fig. 5. Schematic diagram showing the overall solution procedure and coupling between the electrochemical and thermal models.

average product value of the heat capacity and the density:

$$\rho C_P = \frac{\sum_i \rho_i C_{P,i} V_i}{\sum_i V_i}. \quad (13)$$

3.4. Electrochemical-thermal coupling

The battery temperature change during operation affects the electrochemical parameters such as the diffusion coefficients and electrochemical reaction rate constants. Therefore, the thermal and electrochemical models are highly coupled. To couple these models, the method suggested by Song and Evan [43] is adopted. A schematic of this procedure is presented in Fig. 5. In this method, assuming a quasi-steady-state temperature at each time step, the electrochemical model is solved at a fixed temperature yielding the heat generation over the specified time step. The electrochemical heat generation and heat generated in the current collectors are then used in the thermal model to calculate a new temperature distribution in the pouch cell. Finally, the new temperature distribution updates the electrochemical parameters utilized in the next time step electrochemical model. Moreover, in order to make sure that the quasi-steady-state assumption holds throughout the simulation, the temperature variation along each time step is monitored. If the temperature variation at any point in the pouch cell exceeds 1 °C, that time step is halved and repeated.

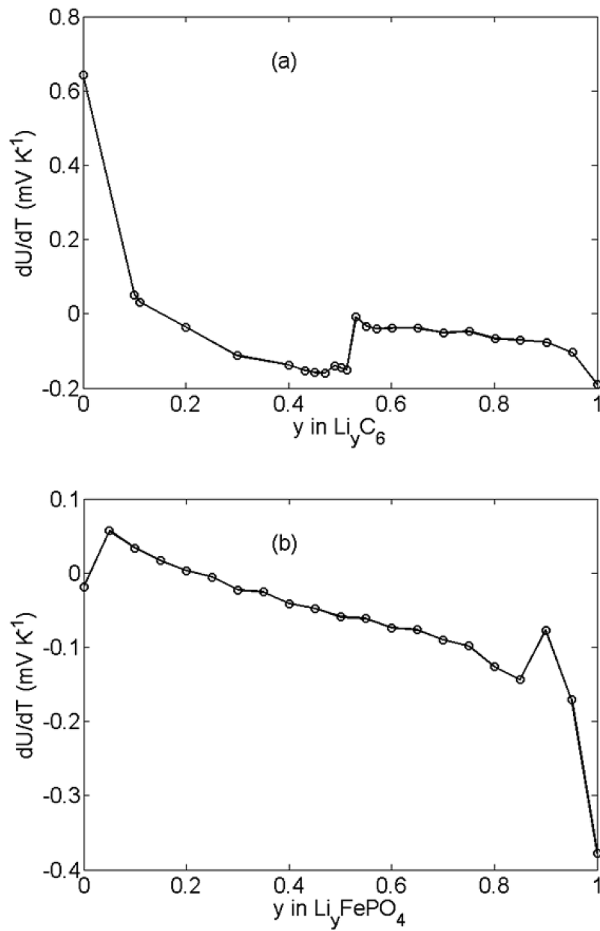


Fig. 6. The equilibrium voltage temperature dependency of the (a) graphite electrode [44] and (b) LFP electrode [45] as a function of lithium concentration.

4. Model parameters

The required electrochemical parameters for the electrodes and separator and their temperature dependencies are obtained from Li/graphite and Li/LFP half-cell simulations as reported in Ref. [36]; therefore, are not repeated here. The low and high cut-off voltages for the pouch cell are set to 2.4 V and 3.7 V, respectively (the 3.7 V limit is a manufacturer's recommendation, and the 2.4 V limit is an experimental apparatus limitation). The temperature dependency of the electrodes equilibrium voltage is approximated using the data reported in the literature. In order to be consistent with the half-cell simulations presented in Ref. [36], the data reported by Reynier et al. [44] is used for the graphite equilibrium voltage temperature dependency and the data given by Dodd et al. [45] is utilized for the LFP equilibrium voltage temperature dependency. These temperature dependencies are given in Fig. 6-a and Fig. 6-b for graphite and LFP electrodes, respectively. As explained in Ref. [36], for the temperature range studied in this paper, the temperature dependency of the equilibrium voltages is negligible. However, they contribute significantly to the heat generation in active material layers as discussed in Section 3.3.2.

In addition to the electrochemical parameters, the geometric parameters of the negative and positive double-sided electrodes in the pouch cell are given in Fig. 7. To measure these parameters the pouch cell was cut and disassembled inside a glove box. The thickness of each layer in the pouch cell is also given in Table 2. The separator and casing thicknesses were measured using a micrometer while the thicknesses of other layers are obtained from Ref. [36]. The parameters required for the thermal modeling of the pouch cell include the density, heat capacity, and thermal conductivity of battery materials, as well as the

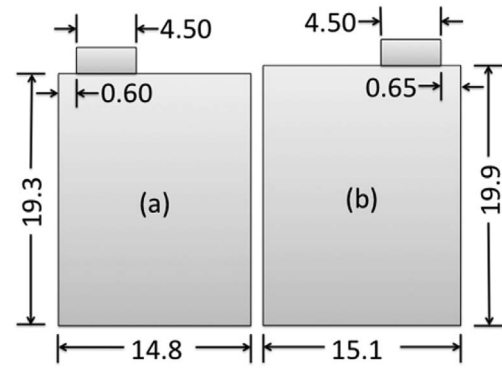


Fig. 7. The geometric parameters of (a) the negative electrode and (b) the positive electrode. All dimensions are in cm.

Table 2

Thicknesses and thermal properties of LIB components (m: measured, ma: Mastali et al. [36], li: Li et al. [46], ch: Chen et al. [42], ta: Taheri et al. [47]).

Material	Thickness, L , (μm)	Density, ρ , (kg m^{-3})	Heat capacity, C_p , ($\text{J kg}^{-1} \text{K}^{-1}$)	Thermal conductivity, k , ($\text{W m}^{-1} \text{K}^{-1}$)
Graphite	46 ^{ma}	2223 ^{li}	641 ^{li}	1.04 ^{li}
Separator	20 ^m	900 ^{li}	1883 ^{li}	0.5 ^{li}
LFP	59 ^{ma}	1500 ^{li}	800 ^{li}	1.48 ^{li}
Electrolyte		1210 ^{li}	1518 ^{li}	0.099 ^{li}
Copper	10 ^{ma}	8933 ^{ch}	385 ^{ch}	398 ^{ch}
Aluminum	19 ^{ma}	2702 ^{ch}	903 ^{ch}	238 ^{ch}
Casing	110 ^m	1150 ^{ta}	1900 ^{ta}	0.16 ^{ta}

electrical conductivity of current collectors, and are listed in Table 2. Finally, the electrical conductivities of the copper and aluminum current collectors in S cm^{-1} are given by Equations (14) and (15) [41]:

$$\sigma_{Cu} = -0.04889T^3 + 54.65T^2 - 21800T + 3.52 \times 10^6 \quad (14)$$

$$\sigma_{Al} = -0.0325T^3 + 37.07T^2 - 1500T + 2.408 \times 10^6 \quad (15)$$

4.1. Stoichiometry window for graphite and LFP electrodes

Given the graphite and LFP electrochemical parameters from half-cell simulations as presented above, the two electrodes can now be combined to simulate a complete 20 Ah pouch cell or complete pouch. To this end, however, the initial stoichiometries of the electrodes must first be estimated. When the pouch cell is assembled for the first time, the LFP cathode is fully lithiated while the graphite (anode) is completely empty of lithium. During the first charge of the pouch cell, a portion of the cathode lithium content forms a SEI layer on the surface of the graphite particles [48]. Since the exact amount of lithium consumed for SEI formation is unknown, the initial stoichiometry of the electrodes cannot be calculated. In addition, the stoichiometry window of each electrode during full charge/discharge depends on the capacity ratio of the electrodes [49].

To estimate the initial stoichiometries, the discharge/charge output voltage of the pouch cell at a very slow rate of $C/50$ is simulated using the isothermal 1D model presented in Section 3.1. The simulation of the pouch cell using the 1D model should be valid since the ohmic losses in the current collectors, tabs, etc. are negligible at very low charge/discharge rates; thus, the normal current density distribution between current collectors is almost uniform. The temperature rise of the pouch cell during operation is also insignificant at low C-rates, hence, the isothermal model is satisfactory for this simulation. Since the pouch cell contains 48 cells, the measured electrode dimensions in Fig. 7 yield a total surface area of 1.44 m^2 and 1.37 m^2 for the graphite and LFP electrodes, respectively. The graphite electrode is 5.1% greater in

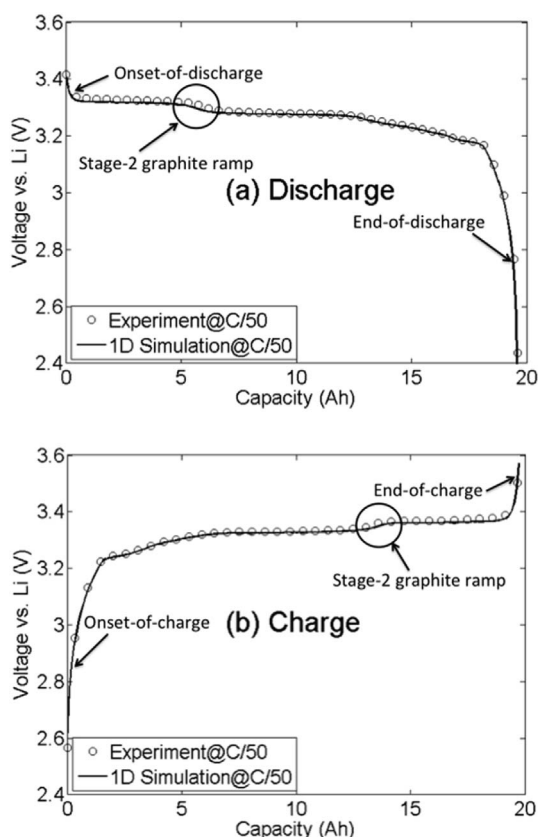


Fig. 8. Fitting the experimental pouch cell voltage curves at C/50 rate using the isothermal 1D model at room temperature (24 °C) during the (a) discharge and (b) charge process.

surface area compared to the LFP electrode for the purpose of preventing lithium plating at the edge of the graphite electrode [50]. This excess graphite area may be inactive, a suggestion that is tested next by allowing the ratio between the graphite and LFP electrode active surface areas to be treated as an adjustable parameter.

Referring to Fig. 8, the initial stoichiometry of the LFP (graphite) electrode during discharge (charge) is estimated by fitting the model to the onset-of-discharge region of the pouch cell voltage data. Similarly, the initial stoichiometry of the LFP (graphite) electrode during charge (discharge) is estimated by fitting the model to the end-of-discharge region voltage data. The initial stoichiometries for discharge and charge are given in Table 3. Finally, the location of stage-2 graphite (Li_yC_{12}) voltage ramp region when fit to the model is used to evaluate the ratio between the graphite and LFP active surface areas. From this curve fit, the ratio between the graphite and LFP active electrode surface areas is determined to be 1.0 suggesting that the 5.2% extra surface area of the graphite electrode is inactive and solely exists for battery safety.

5. Results and discussions

5.1. Model implementation and validation

The equations described in Section 3 are finite volume discretized and implemented using an in-house Fortran code. Since the modeling

Table 3
The initial stoichiometry of electrodes in 20 Ah pouch cells.

	Discharge	Charge
Graphite	0.816	0.003
LFP	0.012	0.941

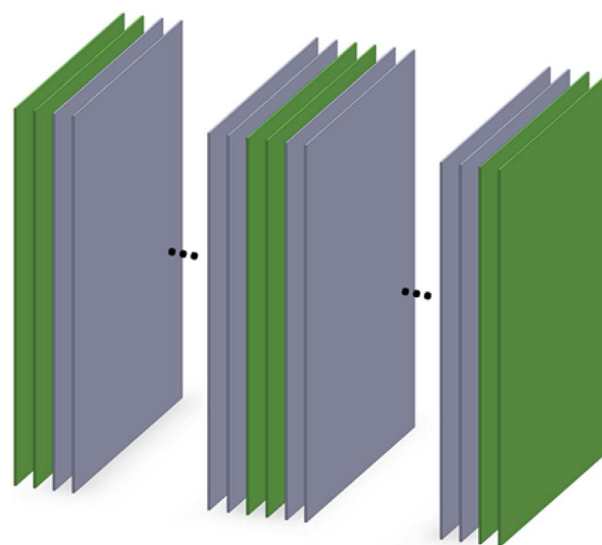


Fig. 9. Shown in green are the six layers used for the current distribution calculations (two on each end, and two in the middle). (For interpretation of the references to colour in this figure legend, the reader is referred to the Web version of this article.)

approach used in this paper requires many calls to the 1D electrochemical model subroutine, a flexible fast Fortran code is preferred over available multi-physics commercial tool as discussed in Ref. [34]. In addition, to improve the code convergence speed, a non-uniform structured grid, which is finer in regions close to the tabs and is coarser further away from the tabs, is used. It is important to note that the tabs are not included in the model, however, they still impact the thermal characteristics of the pouch cell. To capture this impact, the tabs are modelled as a heat source boundary condition at the tab/current collector interface, as explained later in Fig. 12.

Even with the model simplifications detailed above, computations for the 20 Ah pouch cell containing 48 individual cells are still intensive (more than 12 h). Reviewing the 48-cell pouch cell current distribution results, it was observed that the current flowing through the current collectors was virtually the same for all individual cells except for the two on either side of the pouch cell. Since most of the model computational time/cost is related to the current distribution calculation, the model is further simplified by considering only 6 individual cells for the current distribution calculation: the two individual cells on either side of the pouch cell and two representative interior cells (see Fig. 9). This simplification reduces the maximum computation time to less than one hour. In contrast to the current calculation, the thermal modeling is fast and continues to use the full 48 individual cells.

To validate the 20 Ah model, the measured operating voltage and temperature distribution on the surface of the pouch cell are compared with the model voltage and temperature predictions. The experimental method and the temperature sensor locations are described in Section 2 and shown in Fig. 1, respectively. Ambient temperature and initial pouch cell temperature was 24 °C. Experiment and simulation voltage curves under 1C–5C current rates in discharge and charge modes are compared in Fig. 10. The contact resistance between the current collectors and electrodes, R_c , as well as the voltage drop resistance are the only parameters adjusted to obtain these fits. The voltage drop resistance consists of the contact resistance that forms when joining the individual cell tabs into a single pouch cell tab plus the ohmic losses in the tab material itself. The individual cell tabs are joined together through a punch process. As explained in the paragraphs that follow, the current collector/electrode contact resistance is estimated to be $2.0 \times 10^{-4} \Omega \text{ m}^2$, through fitting the model to experiment surface temperatures. Furthermore, the total resistance for the tabs is estimated to be $3.0 \times 10^{-4} \Omega$, which is determined by fitting the model to charge and discharge voltages. As expected, for an increasing tab resistance, the

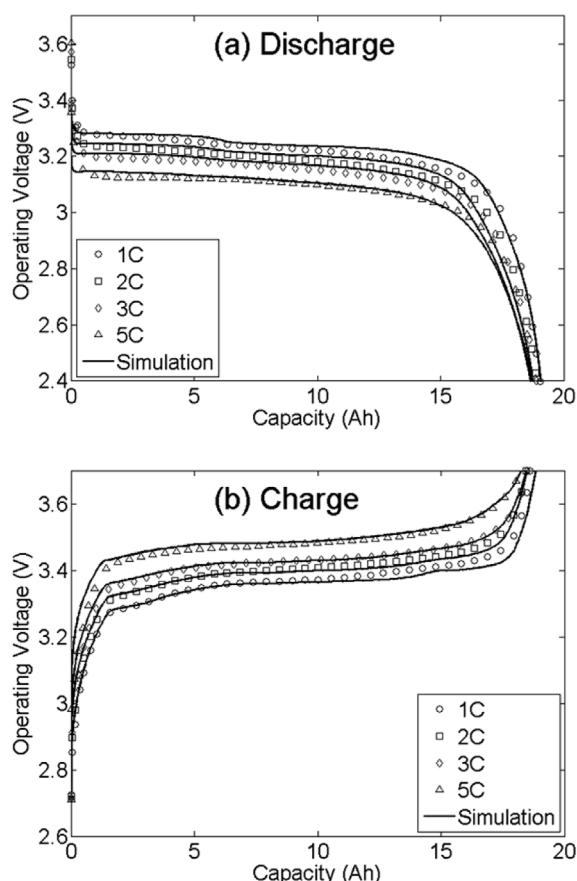


Fig. 10. Comparison between the experimental operating voltages (markers) and simulation results (solid lines) at different (a) discharge and (b) charge rates (1C–5C). Initial pouch cell and ambient temperatures are 24 °C.

voltage curves shift down during discharge and shift up during charge. As shown in Fig. 10, simulation results nicely follow the experimental voltage profiles, with a relative error of less than 3% for charge and 4% for discharge.

To validate the thermal model used, the predicted temperature distribution on the surface of the pouch cell is compared against experimental data. However, it should first be noted that, as seen in Fig. 1, for safety purposes, a safety flush-mounting plug (model ID/S6AR-N-S) [51] is used to connect the tabs to the cables carrying current from the battery cyclers. These plugs are attached to the tabs using a nut and bolt connection that introduce a contact resistance between the cycler cables and the tabs. Fig. 11 shows a close-up top view of the flush-mounting plugs. Even though the tabs are not included in the model, they do experience ohmic heating, and therefore provide a heat flux boundary condition. This heat flux boundary condition is modelled as a heat source at the boundary of the current collector/tab interface. The importance of Fig. 11 is to note that the voltage drop resistance is less than the heat generation resistance responsible for ohmic heating of the tab; that is, the tab voltage is measured before the flush-mounting plug contact resistance. Consequently, in addition to the voltage drop resistance determined above, a heat generation resistance must be determined. The next paragraphs of this section explain how this heat generation resistance is determined.

To have a better understanding of the heat transferred from the tabs toward the battery, two thermocouples are connected to the tabs, and the recorded temperatures are compared with the pouch cell surface temperatures at locations near the tabs. Fig. 12, for instance, shows this comparison during 5C charge/discharge rates. As seen, the tab temperatures are much higher (~50 °C) compared to the points on the pouch cell surface, resulting in a significant heat transfer from the tabs

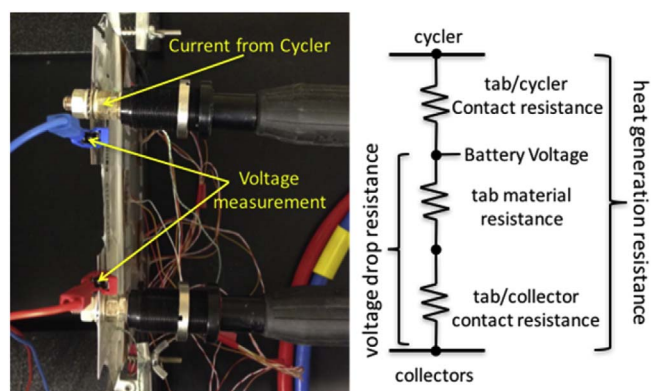


Fig. 11. Location of the voltage measurement as well as the nut and bolt connection utilized to attach the tabs to the battery cycler cables (left), and schematic of the voltage drop and heat generation resistances used to validate the cell voltage and temperature distribution on the surface of the pouch cell (right).

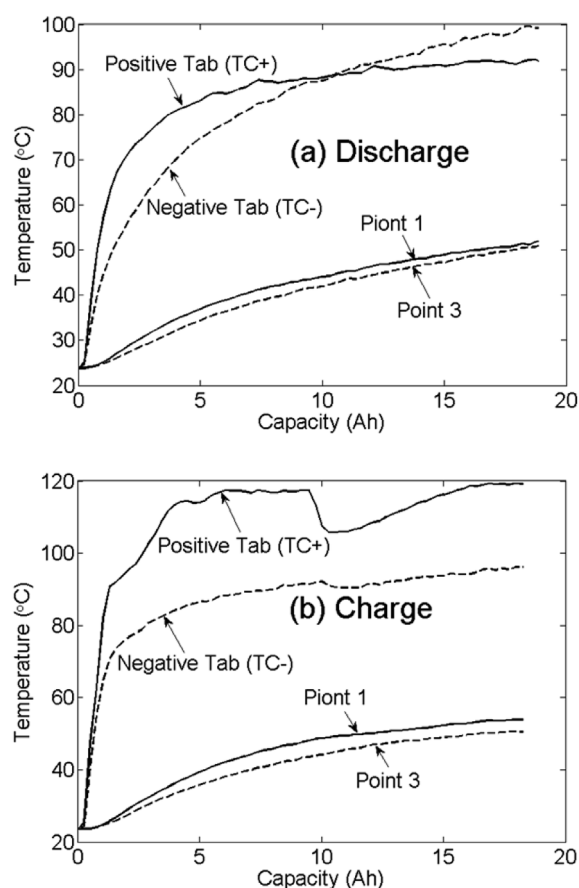


Fig. 12. Comparison between the experimentally measured temperatures at the positive and negative tabs, and at the points closest to the tabs on the pouch cell surface during (a) 5C discharge and (b) 5C charge rates. See Fig. 1 for measurement locations.

toward the cell current collectors. The higher temperature on the tabs, however, is a local measurement made near the point of tab/cycler contact resistance and is expected to reduce due to the temperature gradient observed on the tab [52].

In order to determine the heat generation resistances at the positive and negative tabs as well as the convective heat transfer coefficient, the modelled temperatures at the surface of the pouch cell are fitted to the experimental data. Tab heating has more impact near the tabs, while the effect of convection is more visible away from the tabs. Therefore, the heat generation resistances are fitted with more attention to the battery

temperatures closer to the tabs, while the convective heat transfer coefficient is adjusted with more attention paid to the surface temperatures at the bottom of the pouch cell. This simply means that initially, to speed the fitting process, the heat generation resistances are adjusted based only on the temperature differences measured and modelled near the tabs, and that the convective heat transfer coefficient initially only considered the temperatures at the bottom of the pouch cell. Nevertheless, the fitting process eventually required refinements considering changes to the temperature distribution across the entire cell. The last step prior to fitting the model to experiment is determination of the surface emissivity for radiation heat transfer calculation. Using a Gier-Dunkle DB-100 reflectometer, the emissivity of the pouch cell surface is measured as 0.7.

Using the 5C rate data, following values were fitted for the heat generation resistances at the positive and negative tabs respectively: in discharge process $2.1 \times 10^{-4} \Omega$ and $1.6 \times 10^{-4} \Omega$, and in charge process $2.8 \times 10^{-4} \Omega$ and $2.1 \times 10^{-4} \Omega$. It is important to note that these values are not the actual ohmic resistances of the tabs, but the effective ohmic resistances, which describe the amount of heat transfer from the tab to the cell. How this heat generation resistance is expected to change with the applied current is discussed later in association with Table 4. For now, it is simply observed that trends in the magnitude of the 5C heat generation resistances is consistent with Fig. 12, that is, higher temperature differences correspond to higher heat generation resistances.

The convective heat transfer coefficient is found to be $2 \text{ W m}^{-2} \text{ K}^{-1}$ for both the 5C charge and the 5C discharge processes. This is less than the approximate $4 \text{ W m}^{-2} \text{ K}^{-1}$ for the classic buoyancy flow heat transfer from a vertical flat plate fully exposed to free air flow from the bottom [53]. The reason is that the pouch cell is positioned standing vertically on a flat surface and is therefore not exposed to unconstrained free air flow at the bottom.

Finally, it is important to note that although the heat generation resistances and heat transfer coefficient dominate the fitting process, there is one other parameter that needs to be simultaneously determined: the electrode/collector contact resistance. Since this contact resistance is internal to the pouch cell, it is constant for all C-rates and is estimated to be $2.0 \times 10^{-4} \Omega \text{ m}^2$. This value is necessarily determined by considering all charge/discharge rates since its constant nature is what enables this resistance to be distinguished from the heat transfer coefficient resistance. Fig. 13 compares the simulation results and experiment data during the 5C charge/discharge processes. It is observed that the model is well capable of following the experimental data.

Similar to the fitting procedure described for the 5C charge/discharge rates, the experiment data at other C-rates is fitted using the model. The results at point 5 on the surface of the pouch cell (see Fig. 1) at different charge/discharge rates are presented in Fig. 14, which confirms the model capability in predicting the experiment data for all operating rates. Two error trends are revealed by Figs. 13 and 14. Specifically, Fig. 13 reveals that for a given C-rate errors are larger near the tabs, while according to Fig. 14, for a given location errors are approximately the same for all C-rates. The likely source of the increased error near the tabs is that the model assumes a constant heat flux from the tabs corresponding to a constant temperature difference between the tabs and the cell, whereas in reality, as illustrated in Fig. 12, the temperature difference does change during charging or

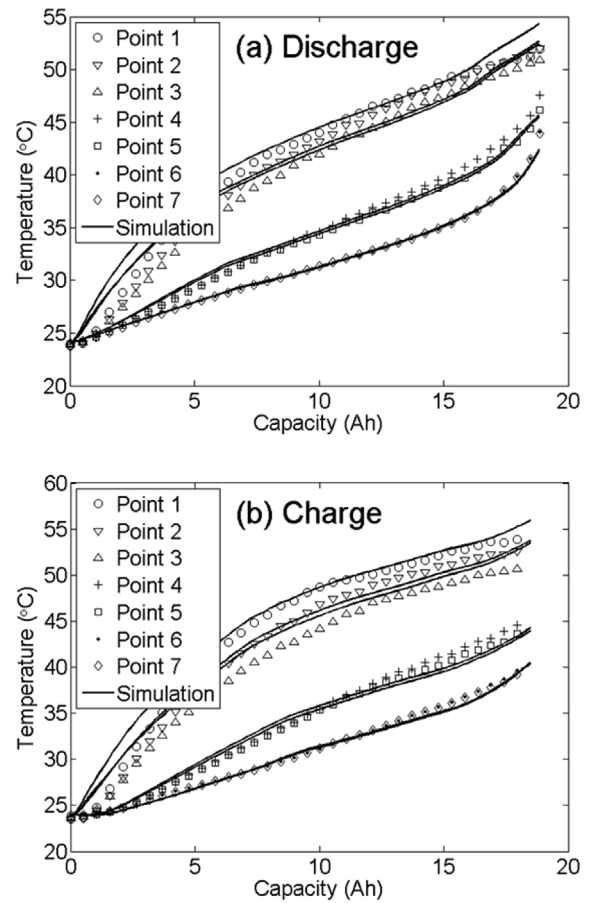


Fig. 13. Comparison between the measured temperatures at different locations on the pouch cell surface (markers) and simulation results (solid lines) at 5C (a) discharge and (b) charge rate. Initial pouch cell and ambient temperatures are 24°C .

discharging.

Results of the fitting process described above for the full range of charge/discharge rates are summarized in Table 4. As expected, the heat transfer coefficient increases with increasing C-rate since the Rayleigh number [53] increases due to the higher surface temperature at higher C-rates. Correspondingly, at higher C-rates with more heat being lost by the tabs through convection a lower percentage of the heat generated in the tabs is conducted to the battery. Therefore, heat generation resistance is expected, and observed, to decrease with increasing C-rate.

5.2. Temperature effect on the pouch cell performance

As shown in Fig. 10, during both charge and discharge, the end capacities are almost independent of charge/discharge rate. This contrasts with the observations for LFP half cells, assembled using the same pouch electrode materials, as shown in Fig. 15 where the end capacities are a strong function of charge/discharge rate [36]. Safari and Delacourt [50,54] made a similar Ah end capacity observation between half

Table 4

Convective heat transfer coefficient, and heat generation resistances at positive and negative tabs, for different discharge and charge rates.

	1C		2C		3C		5C	
	discharge	Charge	discharge	Charge	discharge	Charge	discharge	Charge
Heat transfer coefficient, h , ($\text{W m}^{-2} \text{ K}^{-1}$)	0.8	1.3	1.65	2				
Positive tab resistance, (Ω)	7.0×10^{-4}	1.1×10^{-3}	4.3×10^{-4}	5.6×10^{-4}	3.1×10^{-4}	4.9×10^{-4}	2.1×10^{-4}	2.8×10^{-4}
Negative tab resistance, (Ω)	2.3×10^{-4}	3.5×10^{-4}	1.9×10^{-4}	3.1×10^{-4}	1.9×10^{-4}	3.1×10^{-4}	1.6×10^{-4}	2.1×10^{-4}

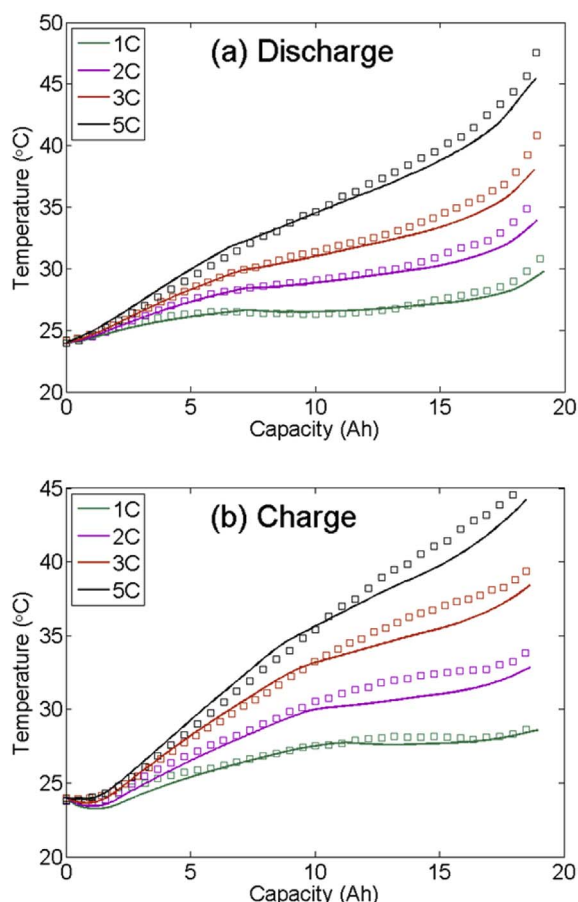


Fig. 14. Measured temperatures at the pouch cell surface (markers) at point 5 (shown in Fig. 1) versus simulation results (solid lines) at different (a) discharge and (b) charge rates of 1C, 2C, 3C, and 5C with the initial cell and ambient temperatures of 24 °C.

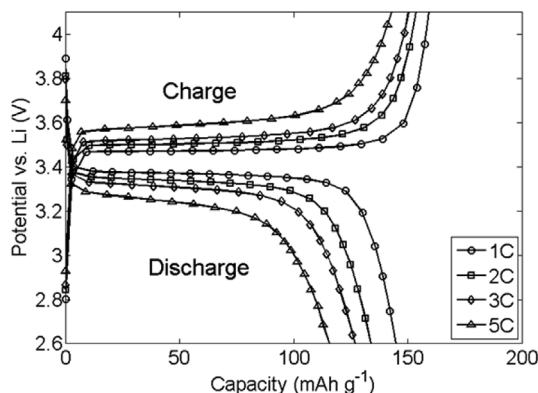


Fig. 15. Experimental galvanostatic charge/discharge voltage for the operating rates ranging from 1C to 5C and at temperature of 23 °C.

cells and pouch cells. They suggested that the pouch cells have a higher uniaxial pressure that correspondingly decreases the contact resistance between the LFP particles and conductive matrix; thus, yielding electrode Ah performance improvement for pouch cells in comparison to half cells. However, it will be proposed in the next paragraph that the dominant reason for such an observation is rather related to a temperature phenomenon than contact resistance.

Isothermal simulations at 5C charge/discharge rates, for the pouch cell at 24 °C and 45 °C, show that cell Ah capacity significantly decreases with decreasing the temperature, especially in the discharge process (Fig. 16). Simulation results for the pouch cell without the

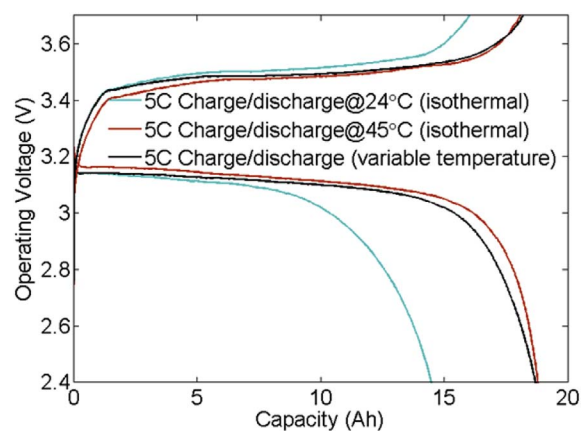


Fig. 16. Impact of discharge rate and temperature on the pouch cell end-capacity.

isothermal constraint are also shown in Fig. 16. A close inspection of Fig. 16 reveals that the operating voltage of the non-isothermal pouch cell, which is initially at the ambient temperature of 24 °C, as expected, starts to follow the voltage profile of the 24 °C isothermal cell. However, as the non-isothermal pouch cell starts to heat up, the voltage profile shifts to follow the 45 °C voltage trace. This strongly suggests that the Ah capacity performance improvement seen in pouch cells over corresponding small LFP cells is due to the temperature increase from internal heating that is significant in the layered pouch cell, but mostly absent in the much smaller one-layer cells. Therefore, the capacity improvement is dominated by temperature effects and not contact resistance as proposed by Safari and Delacourt [54]. This observation can be attributed to the temperature dependency of the electrodes kinetic and transport properties, especially the LFP electrode diffusion coefficient.

5.3. Temperature distribution and heat generation simulations

The heat generation rate in the active material layers and current collectors of the 24th cell (middle or center cell) of the pouch cell is shown in Fig. 17 and Fig. 18, respectively. As seen in Fig. 17, the heat generation rate in the active material layers considerably varies with time or Ah capacity as well as the location on the cell. This is partially due to the variations in both normal current density crossing the layers and local SOC of active materials. In addition to ohmic heating, the active material layers experience entropic heat generation which explains the sharp rise in heat generation seen in Fig. 17 towards the end of charge or discharge. The entropic heat is also responsible for the initial cooling seen in Fig. 17-b for charging.

In the case of current collectors, since the current flowing inside the current collectors is almost constant over time, the heat generation rate does not change during the battery operation. In addition, between the charge and discharge processes, only the current direction varies and its value remains constant. Therefore, the heat generation rate in the current collectors of the 24th cell is shown solely for the middle of the discharge process. Fig. 18 illustrates that the heat generated close to the current collector tabs is larger compared to the other parts due to the higher current density at those locations. Except those regions, the heat generation rate in other current collector locations is insignificant.

Fig. 19 shows the temperature distribution in the 24th cell of the pouch cell in the middle and end of discharge and charge, for the 5C rates and initial cell and ambient temperatures of 24 °C. Temperatures close to the tabs are higher in comparison to those at other locations, and especially in comparison to the temperatures at the bottom of the cell. The higher temperature near the tabs is mostly attributed to the larger ohmic heating in the tabs and current collectors due to the higher current density. Recall, heating in the tab is a heat source for the pouch cell.

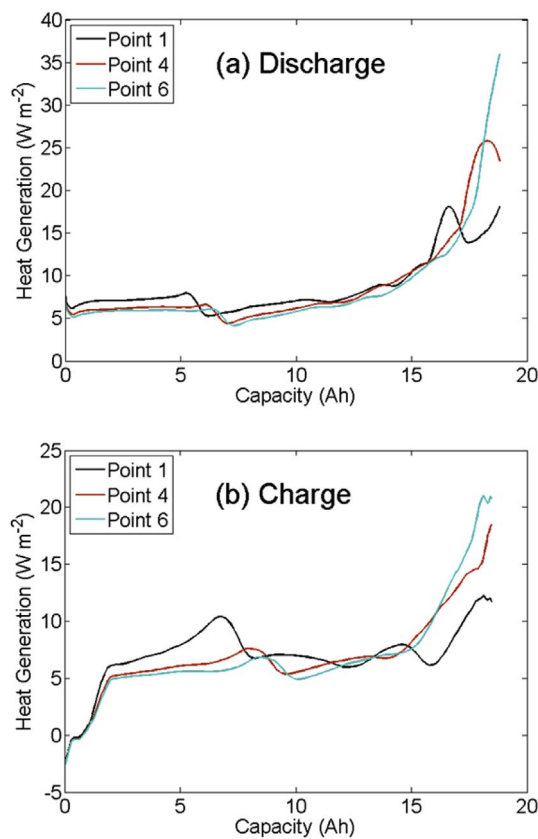


Fig. 17. Heat generation in the 24th active material layers of the pouch cell for three representative points on top, middle, and bottom of the cell during the 5C rate (a) discharge and (b) charge with the initial cell and ambient temperatures of 24 °C.

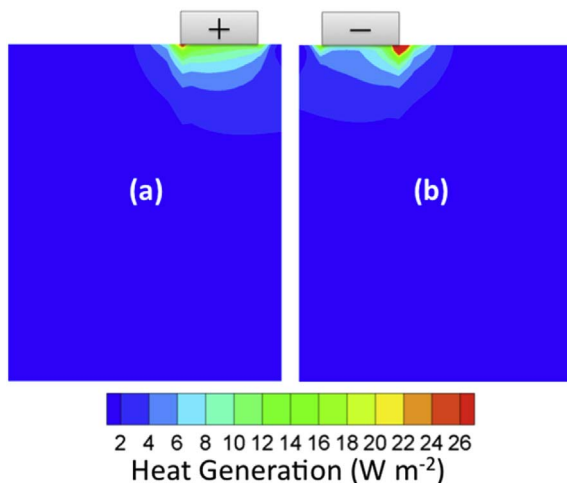


Fig. 18. Heat generation rate for (a) positive and (b) negative current collectors of the 24th cell of the pouch cell when half discharged at the 5C discharge rate, and with ambient and initial cell temperatures of 24 °C.

Fig. 20 shows the temperature of three representative points at the top, middle, and bottom of the 24th cell or the center cell (points 1, 4, and 6 in Fig. 1, respectively) for the same operating conditions as before. As expected, the temperature at the center is always higher than the temperature at the surface of the cell. For this relatively thin pouch cell, however, the temperature difference between the center and surface does not exceed 2 °C. It must be remembered that the heat transfer mechanism is assumed to be free convection, with a convection coefficient of $2 \text{ W m}^{-2} \text{ K}^{-1}$ for the 5C rate. In the case of forced convection, a greater temperature difference between the center and surface of the

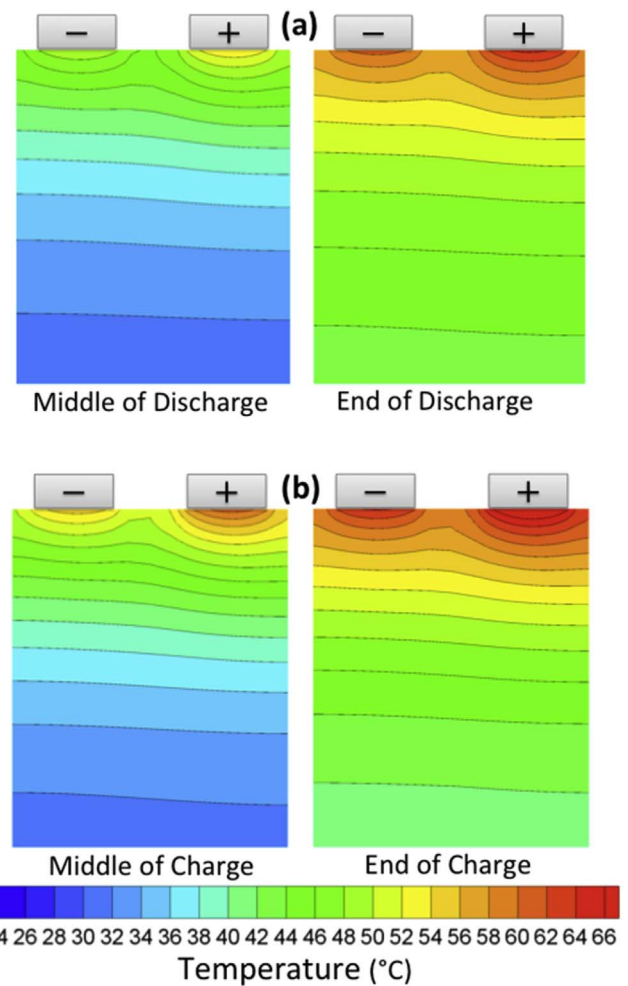


Fig. 19. The temperature distribution on the 24th cell of the pouch cell in the middle and end of 5C (a) discharge and (b) charge with the initial cell and ambient temperatures of 24 °C.

pouch cell would be expected. For example, when the convection coefficient is increased tenfold to $20 \text{ W m}^{-2} \text{ K}^{-1}$, a maximum center to surface temperature difference of 3 °C is predicted by the model. This temperature difference is still small relative to the temperature increase seen within the pouch cell during charge or discharge (see Fig. 13). This finding suggests that the LIB surface temperature is a good representative of the battery center temperature. Hence, to control the battery temperature and improve its durability, monitoring the maximum surface temperature occurring close to the tabs would provide the necessary information for the battery control unit. This would help the manufacturers to minimize the number of required sensors.

6. Conclusions

A high-fidelity electrochemical-thermal model for a 20 Ah pouch cell is developed and validated against the experimental data for charge/discharge rates ranging from 1C (20 A) to 5C (100 A). Physics-based 1D electrochemical models are coupled with charge conservation and heat diffusion equations to describe the electrochemical, electrical, and thermal variables distribution all throughout the LIB domain. Unique to this work is the simultaneous and detailed incorporation of important factors, such as heat generation in the current collectors, heat from current collector tabs, and the reversible entropic heat generation. The accuracy of the model, in predicting the cell output voltage and the temperature distribution on the surface of the pouch cell, confirms the applicability of the model for other LIB materials and geometries. In

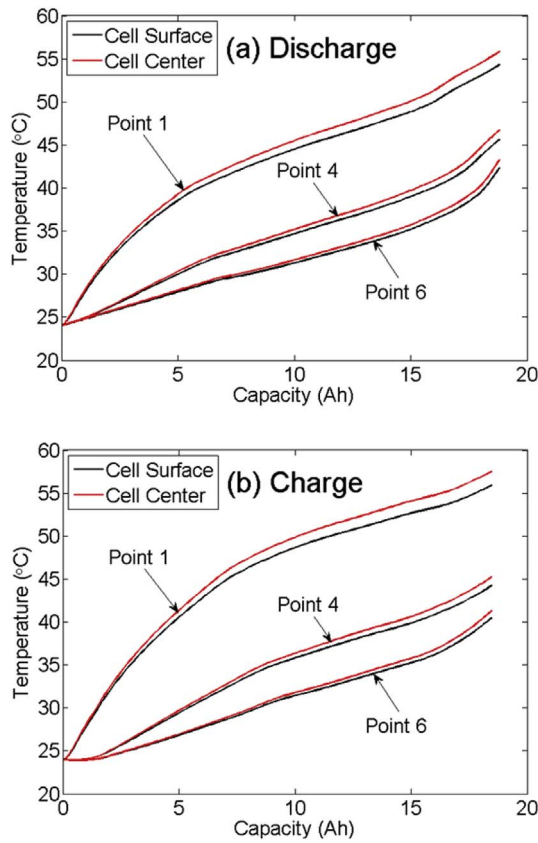


Fig. 20. Comparing the temperatures at the center and surface of the pouch cell for three representative points on top, middle, and bottom of the cell during the 5C (a) discharge and (b) charge with the initial cell and ambient temperatures of 24 °C.

this model, all the electrochemical properties of the graphite and LiFePO_4 electrodes and their temperature dependence are obtained from half-cell tests and simulations conducted on the same electrode materials. The rest of parameters such as electrolyte properties and cell dimensions are obtained from literature or measurements. Thus, compared to the available LIB models, this high-fidelity modeling approach offers a significant improvement, as the model fitted parameters are actually representative of the physical phenomena in an LIB.

Using the developed model, it is shown that the improved electrochemical performance of large-sized pouch cells compared to the small cells is mainly due to the improved kinetic and transport properties of the electrodes, not reduced contact resistances as suggested in the literature. It is found that the improved kinetic and transport properties is the result of self-heating and subsequent increased internal temperature of large-sized pouch cells, which is negligible in the case of small cells. Afterwards, the temperature and heat generation distributions of the pouch cell during charge and discharge are discussed. It is shown that close to the tabs heat is generated from both current collectors and active material layers, while far from the tabs active material layers are the only source of heat generation. Finally, simulation results reveal that in the case of pouch cells, the temperature gradient across the thickness of a multi-layer cell is negligible. For example, even at high charge/discharge rates and with high heat transfer coefficients at the surface of the pouch cell, the temperature gradient across the cell does not exceed 3 °C. Therefore, it is suggested that for the thermal management systems and control applications utilizing a single temperature sensor close to the battery tabs would provide sufficient information regarding the battery thermal behavior.

It is believed that the presented model can further be utilized to even study the effect of the nano-particle shape and size as well as electrode and electrolyte properties on the operation of large-sized LIBs,

thanks to its capability in physics-based modeling of the particle and electrode level phenomena.

Acknowledgement

The authors would like to acknowledge The Natural Sciences and Engineering Research Council of Canada (NSERC) (NSERC CRD - CRDPJ 461493-13), The University of Akron, and Transport Canada (T8125-09001S/001/XSB) for financial support of this research project.

Nomenclature

A	surface area, m^2
a	slope of the linear current-voltage relation, S m^{-2}
a_k	specific surface area of the k^{th} active particle bin, m^{-1}
b	y-intercept of the linear current-voltage relation, A m^{-2}
C_p	specific heat, $\text{J kg}^{-1} \text{K}^{-1}$
c_e	electrolyte concentration, mol m^{-3}
c_e^0	initial electrolyte concentration, mol m^{-3}
$c_{s,k}$	Li concentration inside the k^{th} active particle bin, mol m^{-3}
$c_{s,k}^0$	initial Li concentration inside the k^{th} active particle bin, mol m^{-3}
c_s^{max}	maximum Li concentration in active particles, mol m^{-3}
\mathcal{D}	solid-state binary diffusion coefficient, $\text{m}^2 \text{s}^{-1}$
D_e	electrolyte diffusion coefficient, $\text{m}^2 \text{s}^{-1}$
E	Emissivity
F	Faraday's constant, $96,487 \text{ C mol}^{-1}$
h	convective heat transfer coefficient, $\text{W m}^{-2} \text{K}^{-1}$
I_{app}	total current applied to the pouch cell, A
I_i	current flows in the positive current collector/tab interface, A
i_k^0	exchange current density of the k^{th} active particle bin, A m^{-2}
$i_{n,k}$	reaction current density at the surface of the k^{th} active particle bin, A m^{-2}
j_n	electrochemical current generation (normal current density), A m^{-2}
k^0	electrochemical reaction constant, $\text{mol m}^{-2} \text{s}^{-1}$ ($\text{mol m}^{-3})^{-1.5}$
k	thermal conductivity, $\text{W m}^{-1} \text{K}^{-1}$
L	component thickness, m
\dot{q}_{gen}	heat generation per unit volume, W m^{-3}
\dot{q}_{conv}	convective heat transfer per unit surface area, W m^{-2}
\dot{q}_{rad}	radiative heat transfer per unit surface area, W m^{-2}
r_k	radial distance from the center of the k^{th} active particle bin, m
R	universal gas constant, $8.314 \text{ J mol}^{-1} \text{K}^{-1}$
R_c	contact resistance between the electrodes and current collectors, Ωm^2
$R_{p,k}$	radius of the k^{th} active particle bin, m
t	time, s
T	temperature, K
t_+^0	Li^+ transference number
U_k	equilibrium voltage of the k^{th} active particle bin vs. Li, V
V	volume of a specific component, m^3
x	distance from the negative current collector/anode interface inside the cell, m
y_k	mole fraction of the Li concentration in the k^{th} active particle bin
α_k	thermodynamic factor of the k^{th} active particle bin
β	charge-transfer coefficient of the electrode
γ	Bruggeman exponent, 1.5
ε	component porosity
ε_k	volume fraction of the k^{th} active particle bin per unit volume of the electrode
η_k	surface overvoltage of the k^{th} active particle bin, V
ρ	density, kg m^{-3}
κ	ionic conductivity of the electrolyte, S m^{-1}

Φ	electrical voltage of the current collectors, V
ϕ_s	electrical voltage of the electrode, V
ϕ_e	electrical voltage of the electrolyte, V
σ	bulk electronic conductivity, S m^{-1}

Subscript

<i>a</i>	anode
<i>amb</i>	ambient
<i>Al</i>	aluminum
<i>c</i>	cathode
<i>cc</i>	current collector
<i>Cu</i>	copper
<i>lay</i>	active material layers (electrodes plus separator)
<i>layer</i>	a particular layer of the pouch cell
<i>par</i>	parallel
<i>s</i>	separator
<i>ser</i>	series
<i>surf</i>	surface of the pouch cell
<i>X</i>	along the X-axis
<i>Y</i>	along the Y-axis
<i>Z</i>	along the Z-axis

Superscript

<i>eff</i>	effective value
------------	-----------------

References

- [1] D. Doughty, E.P. Roth, A general discussion of Li ion battery safety, The Electrochemical Society Interface 21 (2012) 37–44.
- [2] E. Samadani, M. Mastali, S. Farhad, R.A. Fraser, M. Fowler, Li-ion battery performance and degradation in electric vehicles under different usage scenarios, Int J Energy Res 40 (3) (2015) 379–392.
- [3] M. Safari, C. Delacourt, Aging of a commercial graphite/LiFePO₄ cell, J Electrochem Soc 158 (2011) A1123–A1135.
- [4] R.A. Leising, M.J. Palazzo, E.S. Takeuchi, K.J. Takeuchi, A study of the overcharge reaction of lithium-ion batteries, J Power Sources 97–98 (2001) 681–683.
- [5] W. Cai, H. Wang, H. Maleki, J. Howard, E. Lara-Curzio, Experimental simulation of internal short circuit in Li-ion and Li-ion-polymer cells, J Power Sources 196 (2011) 7779–7783.
- [6] R. Zhao, J. Liu, J. Gu, The effects of electrode thickness on the electrochemical and thermal characteristics of lithium ion battery, Appl Energy 139 (2015) 220–229.
- [7] W. Du, A. Gupta, X. Zhang, A.M. Sastry, W. Shyy, Effect of cycling rate, particle size and transport properties on lithium-ion cathode performance, Int J Heat Mass Tran 53 (2010) 3552–3561.
- [8] Y. Han, L. Dong, J. Feng, D. Li, X. Li, S. Liu, Cobalt oxide modified porous carbon anode enhancing electrochemical performance for Li-ion batteries, Electrochim Acta 167 (2015) 246–253.
- [9] H. Shu, X. Wang, W. Wen, Q. Liang, X. Yang, Q. Wei, et al., Effective enhancement of electrochemical properties for LiFePO₄/C cathode materials by Na and Ti co-doping, Electrochim Acta 89 (2013) 479–487.
- [10] H. Sun, R. Dixon, Development of cooling strategy for an air cooled lithium-ion battery pack, J Power Sources 272 (2014) 404–414.
- [11] W. Tong, K. Somasundaram, E. Birgersson, A.S. Mujumdar, C. Yap, Numerical investigation of water cooling for a lithium-ion bipolar battery pack, Int J Therm Sci 94 (2015) 259–269.
- [12] R. Zhao, J. Gu, J. Liu, An experimental study of heat pipe thermal management system with wet cooling method for lithium ion batteries, J Power Sources 273 (2015) 1089–1097.
- [13] C. Lin, S. Xu, G. Chang, J. Liu, Experiment and simulation of a LiFePO₄ battery pack with a passive thermal management system using composite phase change material and graphite sheets, J Power Sources 275 (2015) 742–749.
- [14] M. Mastali, J. Vazquez-Arenas, R. Fraser, M. Fowler, S. Afshar, M. Stevens, Battery state of the charge estimation using kalman filtering, J Power Sources 239 (2013) 294–307.
- [15] E. Samadani, S. Farhad, W. Scott, M. Mastali, L.E. Gimenez, M. Fowler, et al., Empirical modeling of lithium-ion batteries based on electrochemical impedance spectroscopy tests, Electrochim Acta 160 (2015) 169–177.
- [16] M. Mastali Majdabadi, S. Farhad, M. Farkhondeh, R.A. Fraser, M. Fowler, Simplified electrochemical multi-particle model for LiFePO₄ cathodes in lithium-ion batteries, J Power Sources 275 (2015) 633–643.
- [17] M. Guo, R.E. White, A distributed thermal model for a Li-ion electrode plate pair, J Power Sources 221 (2013) 334–344.
- [18] C. Veth, D. Dragicevic, R. Pfister, S. Arakkan, C. Merten, 3D electro-thermal model approach for the prediction of internal state values in large-format lithium ion cells and its validation, J Electrochem Soc 161 (2014) A1943–A1952.
- [19] K.H. Kwon, C.B. Shin, T.H. Kang, C.-S. Kim, A two-dimensional modeling of a lithium-polymer battery, J Power Sources 163 (2006) 151–157.
- [20] U.S. Kim, J. Yi, C.B. Shin, T. Han, S. Park, Modeling the dependence of the discharge behavior of a lithium-ion battery on the environmental temperature, J Electrochem Soc 158 (2011) A611–A618.
- [21] T. Bandhauer, S. Garimella, T.F. Fuller, Electrochemical-thermal modeling to evaluate battery thermal management strategies: I. Side cooling, J Electrochem Soc 162 (2014) A125–A136.
- [22] Y. Lai, S. Du, L. Ai, L. Ai, Y. Cheng, Y. Tang, et al., Insight into heat generation of lithium ion batteries based on the electrochemical-thermal model at high discharge rates, Int J Hydrogen Energy 40 (2015) 13039–13049.
- [23] W. Huo, H. He, F. Sun, Electrochemical-thermal modeling for a ternary lithium ion battery during discharging and driving cycle testing, RSC Adv 5 (2015) 57599–57607.
- [24] X. Zhang, X. Chang, Y. Shen, Y. Xiang, Electrochemical-electrical-thermal modeling of a pouch-type lithium ion battery: an application to optimize temperature distribution, J. Energy Storage. 11 (2017) 249–257.
- [25] M. Xu, Z. Zhang, X. Wang, L. Jia, L. Yang, A pseudo three-dimensional electrochemical-thermal model of a prismatic LiFePO₄ battery during discharge process, Energy 80 (2015) 303–317.
- [26] J. Li, Y. Cheng, L. Ai, M. Jia, S. Du, B. Yin, et al., 3D simulation on the internal distributed properties of lithium-ion battery with planar tabbed configuration, J Power Sources 293 (2015) 993–1005.
- [27] D. a. H. McCleary, J.P. Meyers, B. Kim, Three-dimensional modeling of electrochemical performance and heat generation of spirally and prismatically wound lithium-ion batteries, J Electrochem Soc 160 (2013) A1931–A1943.
- [28] K.-J. Lee, K. Smith, A. Pesaran, G.-H. Kim, Three dimensional thermal-, electrical-, and electrochemical-coupled model for cylindrical wound large format lithium-ion batteries, J Power Sources 241 (2013) 20–32.
- [29] M. Mastali, E. Samadani, S. Farhad, R.A. Fraser, M. Fowler, Three-dimensional electrochemical analysis of a graphite/LiFePO₄ Li-Ion cell to improve its durability, SAE technical paper 2015-01-1182, vol. 2015, 2015, pp. 1–9.
- [30] E. Samadani, J. Lo, M. Fowler, R.A. Fraser, L. Gimenez, Impact of temperature on the A123 Li-Ion battery performance and hybrid electric vehicle range, (2013).
- [31] LabVIEW System Design Software - National Instruments, LabVIEW system design software - national Instruments, (2016) <http://www.ni.com/labview/>.
- [32] BCS-815 Battery Cycling System - Bio-Logic - Science Instruments, BCS-815 battery cycling system - bio-logic - science Instruments, (2016) <http://www.bio-logic.info/instruments/battery-cycling-bcs-815/>.
- [33] BioLogic science Instruments, (2017) <http://www.bio-logic.net/en/>.
- [34] M. Mastali, E. Samadani, S. Farhad, R.A. Fraser, M. Fowler, Three-dimensional multi-particle electrochemical model of LiFePO₄ cells based on a resistor network methodology, Electrochim Acta 190 (2016) 574–587.
- [35] M. Doyle, T.F. Fuller, J. Newman, Modeling of galvanostatic charge and discharge of the lithium/polymer/insertion cell, J Electrochem Soc 140 (1993) 1526–1533.
- [36] M. Mastali, M. Farkhondeh, S. Farhad, R. Fraser, M. Fowler, Electrochemical modeling of commercial LiFePO₄ and graphite electrodes: kinetic and transport properties and their temperature dependence, J Electrochem Soc 163 (2016) A2803–A2816.
- [37] J. Christensen, D. Cook, P. Albertus, An efficient parallelizable 3D thermoelectrochemical model of a Li-ion cell, J Electrochem Soc 160 (2013) A2258–A2267.
- [38] S.U. Kim, P. Albertus, D. Cook, C.W. Monroe, J. Christensen, Thermoelectrochemical simulations of performance and abuse in 50-Ah automotive cells, J Power Sources 268 (2014) 625–633.
- [39] K.E. Thomas, J. Newman, Thermal modeling of porous insertion electrodes, J Electrochem Soc 150 (2003) A176–A192.
- [40] W. Fang, O.J. Kwon, C. Wang, Electrochemical – thermal modeling of automotive Li-ion batteries and experimental validation using a three-electrode cell, Int J Energy Res 34 (2010) 107–115.
- [41] R.E. Gerver, J.P. Meyers, Three-dimensional modeling of electrochemical performance and heat generation of lithium-ion batteries in tabbed planar configurations, J Electrochem Soc 158 (2011) A835–A843.
- [42] S.C. Chen, C.C. Wan, Y.Y. Wang, Thermal analysis of lithium-ion batteries, J Power Sources 140 (2005) 111–124.
- [43] L. Song, J.W. Evans, Electrochemical-thermal model of lithium polymer batteries, J Electrochem Soc 147 (2000) 2086–2095.
- [44] Y. Reynier, R. Yazami, B. Fultz, The entropy and enthalpy of lithium intercalation into graphite, J. Power Sources (2003) 850–855.
- [45] J.L. Dodd, S. Nishimura, R. Yazami, A. Yamada, B. Fultz, Entropy of lithiation in LiFePO₄, 210th ECS Meeting, Abstract #179 (2006).
- [46] J. Li, Y. Cheng, M. Jia, Y. Tang, Y. Lin, Z. Zhang, et al., An electrochemical-thermal model based on dynamic responses for lithium iron phosphate battery, J Power Sources 255 (2014) 130–143.
- [47] P. Taheri, M. Yazdanpour, M. Bahrami, Transient three-dimensional thermal model for batteries with thin electrodes, J Power Sources 243 (2013) 280–289.
- [48] P. Arora, R. White, M. Doyle, Capacity fade mechanisms and side reactions in lithium-ion batteries, J Electrochem Soc 145 (1998) 3647–3667.
- [49] J. Christensen, J. Newman, Cyclable lithium and capacity loss in Li-Ion cells, J Electrochem Soc 152 (2005) A818.
- [50] M. Safari, C. Delacourt, Mathematical modeling of lithium iron phosphate electrode: galvanostatic charge/discharge and path dependence, J Electrochem Soc 158 (2011) A63.
- [51] Multi-Contact.com, Electrical connectors and contacts by Multi-Contact AG, (2016) <http://www.multi-contact.com/>.
- [52] S. Panchal, I. Dincer, M. Agelin-Chaab, R. Fraser, M. Fowler, Experimental and simulated temperature variations in a LiFePO₄-20 Ah battery during discharge process, Appl Energy 180 (2016) 504–515.
- [53] F.P. Incropera, D.P. DeWitt, Introduction to heat transfer, sixth ed., John Wiley & Sons, 2011.
- [54] M. Safari, C. Delacourt, Modeling of a commercial graphite/LiFePO₄ cell, J Electrochem Soc 158 (2011) A562.